Soft Matter

Microscopic Details of a Fluid/Thin Film Triple Line

SCHOLARONE™
Manuscripts

Soft Matter

ARTICLE TYPE

Microscopic Details of a Fluid/Thin Film Triple Line[†]

Timothy Twohig,[a] Sylvio May[a] and Andrew B. Croll,[*a]

In recent years, there has been a considerable interest in the mechanics of soft objects meeting fluid interfaces (elasto-capillary interactions). In this work we experimentally examine the case of a fluid resting on a thin film of rigid material which, in turn, is resting on a fluid substrate. To simplify complexity, we adapt the experiment to a one-dimensional contact geometry and examine the behaviour of polystyrene and polycarbonate films directly with confocal microscopy. We find that the fluid meets the film in a manner consistent with the Young-Dupré equation when the film is thick, but transitions to what appears similar to a Neumann-like balance when the thickness is decreased. However, on closer investigation we find that the true contact angle is always given by the Young construction. The apparent paradox is a result of macroscopically measured angles not being directly related to true microscopic contact angles when curvature is present. We model the effect with an Euler-Bernoulli beam on a Winkler foundation as well as with an equivalent energy-based capillary model. Notably, the models highlight several important lengthscales and the complex interplay of tension, gravity, and bending in the problem.

1 Introduction

The interplay between capillary interactions and deformable materials has recently drawn great interest from the soft matter community. The focus partly stems from the perceived utility of capillary forces in guiding the assembly of microstructures[1] or even in guiding the folding of origami inspired devices.[2,3] Interest has also grown from the identification of novel phenomena which occur simply because capillary forces are applied to solids compliant enough to be locally distorted.[4–16] A simple example can be seen when a fluid drop is placed on a flat elastic half-space. If the modulus of the elastic substrate is large, the drop adopts the familiar spherical cap shape with a contact angle θ_Y, determined by a balance of surface energies in the horizontal direction. However, if the modulus of the substrate is decreased, the substrate is pulled by the vertical component of the contact line into a cusp shape, reminiscent of the Neumann construction.[7–9]

Decreasing Young's modulus is not the only way to increase deformability; a slender material will also be easily deformed as its thickness is reduced. For example, a drop added to a thin film may lead to bending on the scale of the sheet,[2,3,17] interesting pattern formation,[18–21] or even complete droplet wrapping[22,23]. The critical difference between slender and soft deformations lies

in the fact that slender, high-modulus films strongly resist in plane stretching. The significant resistance to creation of Gaussian curvature in a thin rigid sheet, creates new complexity in understanding how the curved fluid-solid triple line of a droplet meets a sheet which is curved along an orthogonal axis. In this work, we examine the interaction of a fluid with a thin rigid sheet on the microscopic level. We work in one dimension in order to avoid in plane stretching, buckling, and localization.[21] We find that the apparent contact triple line changes continuously from solid-like (Young-Dupré) to fluid-like (Neumann) as the film's thickness is reduced. However, we note that true contact is always Young-like, and force balance arguments constructed from macroscopically observed angles are not always correct. Importantly, we show how film bending, gravity of the fluid substrate, and external tension contribute to the deformation shape and apparent contact angles.

Fluid drops on thin, solid substrates have been studied macroscopically by several researchers, though little effort has been made to reconcile macrocsopic models with the microscale. Russell and co-workers were the first to explore the effect of a fluid drop resting on a film floating on a water bath.[18] The capillary action of a droplet draws the film in towards the droplet, creating a compressive hoop stress which quickly leads to the buckling of the film. The buckling can be modeled through the application of the Föppl-von Kármán equations in a limit where bending is ignored.[19,24] The buckling, while useful in determining the film's modulus, significantly complicates any effort to observe the film/fluid triple-line where film bending is important. This is es-

[a] Department of Physics, North Dakota State University, Fargo, USA. Tel: +1 413 320 3810; E-mail: andrew.croll@ndsu.edu

pecially true if the film is pushed to localization (e.g. if the wrinkles collapse into sharp out of plane folds).[21]

On the other hand, if a droplet is placed on a thin film which has its boundaries fixed no buckling will occur on microscopic scales.[25–29] In this case a drop deforms the film underneath it into a parabolic shape (macroscopically), which can be modeled again with a simplified Föppl-von Kármán equation neglecting bending and any stretching in excess of what is created by the clamped boundaries.[26] Macroscopically this view is quite successful, leading to direct measurements of local strain variation[25,28] and strain dependent surface energies in polymer glasses[27] among other results. However, there is no clear picture of what happens in the film at small lengthscales where stretching and bending may again be important.

In this paper we describe a simple, one-dimensional experiment which significantly reduces complexity and allows a direct observation of the local shape of a thin film in contact with a fluid. In short, a glassy polymer film (polystyrene, PS, or polycarbonate, PC) floating on a fluid surface is placed under a droplet of a second fluid which is deformed into a long straight contact line by a capping glass slide (see Fig. 1). The film's surfaces are located in three dimensions through laser scanning confocal microscopy and contact angles are determined on a microscopic scale. Varying the thickness of the film reveals that the deformation persists even in films on the order of 10's of microns in thickness (Föppl-von Kármán number $\sigma \sim L^2/t^2 \sim 10^4$, where L is the lateral size of the film and t is the film thickness). As the film thickness drops below ~ 1 micron we find the contact becomes altered, reminiscent of the Neumann construction typical of fluid/fluid contact problems. However, quantitatively the Neumann result does not appear to be valid in the range of thicknesses we examine.

The contact can be modeled with a composite capillary/bending model, or equivalently via the Euler-Bernoulli beam coupled to a Winkler foundation. The models aid in the discussion of the experimental results, and offer new insight into related problems. We find the data to be well represented by these simple theories, and we find the theory is consistant with a Young-Dupré force balance occurring at the triple line. This occurs because the film is locally flat at the point of contact (the maximum of the film contour). The film rises accounting for the unbalanced vertical component of the liquid-vapour surface tension, but the contact angles are not simply calculated from surface forces alone. Understanding film shape requires knowledge of the relationship of bending, fluid weight, and film tension. The models highlight several important lengthscales which can be used to qualify dominant features in the problem, which we discuss in relation to several limiting cases (for example tension free films, zero density fluid substrates) which are inaccessible to experiments.

2 Experimental

2.1 Film Preparation

Solutions of polystyrene (PS) were created by dissolving bulk PS (Aldrich, Mw = 192 kg/mol) in toluene. To facilitate imaging, Nile Red fluorescent dye (MP Biomedicals, LLC) was added to the solution. The solutions were between 0.1% and 10% PS by
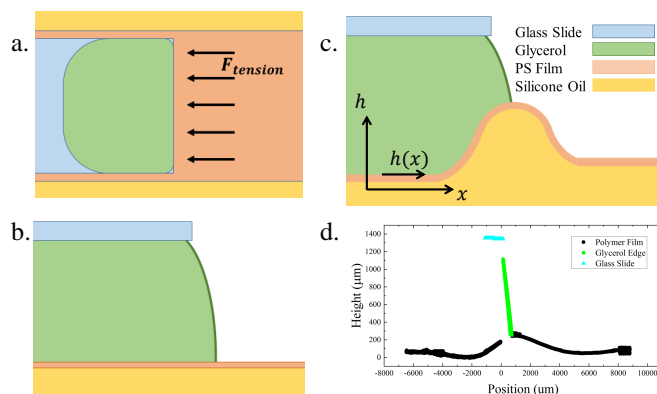

Fig. 1 Schematic of the experimental setup. a.) Top view of the glycerol drop on polymer film floating on oil bath. Glycerol edge is straightened by the glass slide reducing the problem to one-dimension. b.) Side view of the initial setup of the experiment. c.) Side view of the final state of the experiment. d.) Profile data of a real film extracted from the three-dimensional confocal microscope scan of a 4.3 micron thick PC film. Blue represents the glass surface, green the glycerol surface and black is the film and oil surfaces (oil is the thicker line on the right). The gap in the black curve is due to reduced scattering intensity at this resolution. Note the oscillatory profile is strong evidence that film bending cannot be ignored.

weight, depending on the desired film thickness. Polycarbonate (PC) films were created in a similar manner by dissolving bulk PC (Scientific Polymer Products Inc., Mw = 60 kg/mol) in chloroform (Nile Red was also added to these solutions). PC solutions were made between 0.1% and 10% by weight. Thin films were created by spin coating or drop casting the PS or PC solutions onto freshly cleaved mica sheets (Ted Pella, Inc.). Spin coating was used to create polymer samples of thickness 10 nm-700 nm, and drop casting was used to create polymer films of thickness 0.700 μm - 10 μm. Samples were annealed at a temperature of $\sim 30\,°$C above their respective glass transition temperatures. We note, these materials both have high moduli ($E = 3.5$ GPa and 2.2 GPa for PS and PC respectively) and can be considered almost inextensible.[15]

2.2 Film Transfer

The polymer films were cut into rectangular pieces and floated onto a pure water surface (MilliQ, Millipore inc). A slide coated with a high viscosity silicone oil (5100 Cp) and chilled to approximately -20 °C, was gently pressed onto the floating film and removed from the bath taking the film with it. At this point, the film is floating on a silicone oil bath. The sample was allowed to float on the bath overnight in order to relax any stresses that were still present in the film from the floating and lifting process. Film thicknesses were measured by cutting pieces adjacent to the floated films and placing them on silicon wafers. Atomic force microscopy (AFM) was used to measure films of thickness 10 nm-1000 nm. Films thicker than this were imaged with a laser scanning confocal microscope. Reflectance maxima (that corresponded to the top and bottom surfaces of the film) were extracted and were used with the index of refraction for the relevant polymer to find the thickness of each film. Alternatively, the

top surface of a film and the top surface of the substrate could be used near a sample edge. No differences were noted between the various techniques.

A solution of glycerol (99.9% Fisher Chemical) and fluorescent dye (fluorescein sodium, FUL-GLO) was created. A few drops of glycerol solution were deposited on the top of a film floating on (now room temperature) silicon oil, about 1 cm away from the oil-film edge. To create a flat, elongated contact line, a glass slide with an edge parallel to both the film edge and the glycerol line, was placed in contact with the glycerol drops. The geometry is shown in the schematics of Fig. 1a,b. The setup was allowed to equilibrate over two hours, resulting in the state shown in Fig. 1c. The system was then scanned in three-dimensions using confocal microscopy (Olympus FLUOVIEW FV1000), from which the film and glycerol surfaces could be located (Fig. 1d).

2.3 Data Processing

Intensity data was processed using ImageJ software and an algorithm to extract the peak intensity for each vertical slice in the three-dimensional scans. Reflectance and fluorescence channels were separated, allowing discrimination between the glycerol, glass slide, and polymer film surfaces. The height coordinate of submerged portions of films was then corrected to account for the refractive index of glycerol. An example profile with the corrected film heights is given in Fig. 1d. This profile data was used to find the height difference between the oil bath (far right of the film data) and the peak of the deformation.

The relative angles of the glycerol-air interface, film in air, and film submerged in glycerol were extracted from the slopes of the data for these surfaces near the triple point. While data sets span several millimeters, data is often curved on these large scales and therefore fitting the entire dataset with a linear function would be extremely error prone. To avoid the curvature, we focus on a small region starting at the triple line and extending outward along each interface. Specifically, data from the triple point to a distance of $\sim$40 pixels away along the glycerol surface ($\sim$65 μm) is fit. While a distance from the triple point to $\sim$75 pixel along the polymer surface ($\sim$120 μm) is used for fitting. We refer to this length as the observation length for convenience, and denote it with the symbol x_{obs}, which we show in figure 2 for convenience. The number of data points was selected in order to minimize distance from the triple line, while incorporating enough data points to account for noise in the measurements. Obvious out-lying data points were removed by hand (caused by intensity fluctuations for example). Occasionally, the data within x_{obs} of the triple line was indeterminate when fitting an intensity peak. In this case, the data nearest to the triple line where an intensity peak could be reliably fit was used to determine the slope, with the error calculations being adjusted to reflect the shift away from the ideal measurement location. The slopes of the linear fits to the glycerol surface and the polymer surface data were used to calculate the relative angle between the glycerol and polymer surfaces.

3 Results and Discussion

A droplet of glycerol placed on top of a thin film will pull upwards and inwards on the film's surface, deforming the film into the curved shape shown in Fig. 1d. The tension created by the glycerol surface is balanced at the triple line by the interplay of the outward pull of tension in the film, the change in surface energy of the film as the glycerol spreads, and the weight of the fluid displaced below the film. These quantities are also intrinsically linked through bending in the plate as it deforms to accommodate the force balance. If the film is thick, bending becomes the dominant energy, the plate remains flat, and the lift generated at the triple line is balanced by the weight of the fluid beneath the entire plate. If the film is very thin, bending is less relevant, and the amount of fluid lifted is determined by the capillary length ($\sqrt{\gamma_f/\rho g}$, where γ_f is the film's surface energy, ρ is the oil density, and g the gravitational acceleration). We note that in this geometry gravity and bending cannot be ignored in the thin film limit. The main purpose of this paper is to clarify this complex interaction.

Figure 2 shows the surfaces near the fluid/film contact line for a typical thick (3.4 μm) and thin (185 nm) PS film. As it is of macroscopic convenience to discuss contact angles at a triple point, three angles at the contact line are directly measured, α, β, and δ. We sub-divide α and β into a portion above, θ, and below, ϕ, the horizontal for convenience (Fig. 2a). Because we are focusing on small distances from the contact line, angle measurement can often be poorly defined because of the non-zero curvature near the film maxima (note this exact point is made by Davidovitch and Vella[24]). Care must be taken in comparing an apparent angle with any theoretical predictions. We extract angles from theory (discussed below) in the same way as we approach experimental data in order to maintain consistency.

In a thick film (Fig. 2c), the angle β approaches a value of 115°, which is very close to what we measure independently with a sessile glycerol droplet on solid PS film (a PS film of $\sim$ 200 nm which has been spin-coated on an atomically flat silicon substrate, see ESI†). Contact with a thick film can be treated exactly as in the bulk; the contact angle is a result of a horizontal force balance which is independent of any tension in the film caused by external means. In short, the film shows the classical balance of the Young-Dupré law, $\gamma_{sl} + \gamma\cos(\theta_Y) = \gamma_{sv}$, where γ_{sl} and γ_{sv} are the surface energies under the fluid or exposed to air respectively and γ is the glycerol surface tension.

As the film thins, the bending energy is reduced and the contact line deforms and lifts the film, resulting in the angles α and β growing (Fig. 2d). To clarify, α is not equal to θ_Y, and the air-film interface is not horizontal as is often the case with higher tension free-standing films.[25,26,28,29] The glycerol surface, however, remains at a fairly constant angle with respect to the horizontal (see Fig. 3). The measured angle is consistent with θ_Y determined from traditional sessile drop experiments ($\theta = 71 \pm 7°$ for PS and $\theta = 69 \pm 9°$ for PC measured in our experiment). This suggests that the fluid shape is determined by the Young-Dupré balance on a scale much smaller than the local radius of curvature of the film; a lengthscale where the thin polymer film is still effectively
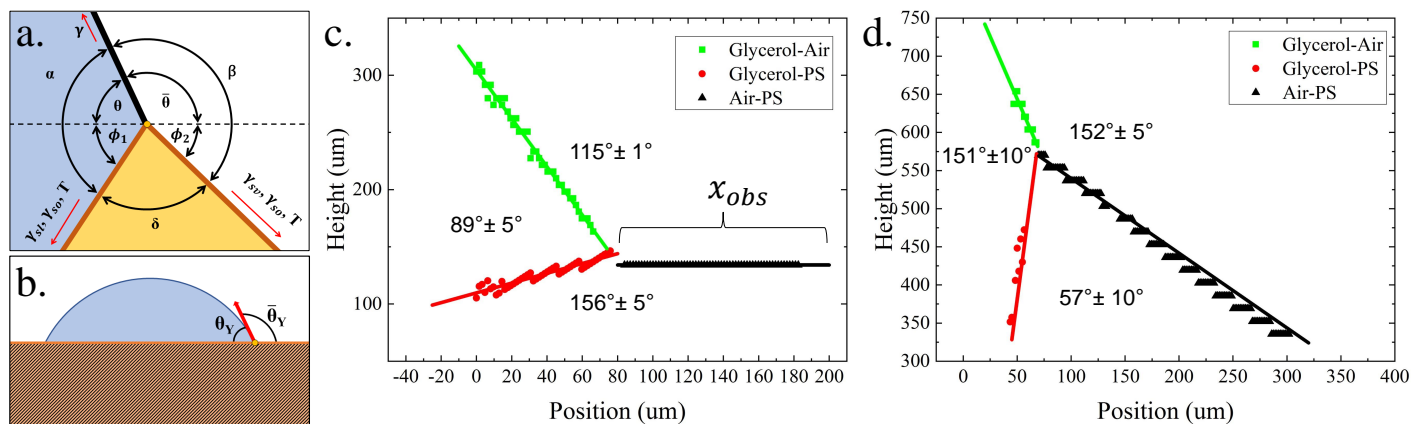
Fig. 2 Surfaces around the triple line. a.) Schematic defining the various angles discussed in the text. b.) The Young-Dupré limit for reference. c.) Experimental measurement of the triple line in a thick (3.4 μm) PS film. Green represents the glycerol surface, black represents the film surface outside the fluid, and red represent the film surface below the glycerol. Solid lines are linear fits over the distance x_{obs} used to determine the angles at the triple line. For comparison, x_T for this film is 7.7×10^{-4} m. d.) Similar measurement with a much thinner film (185 nm). The relative position of the polymer film has changed, while the fluid surface remains in a similar position. In this case, x_T is 9.7×10^{-6} m.
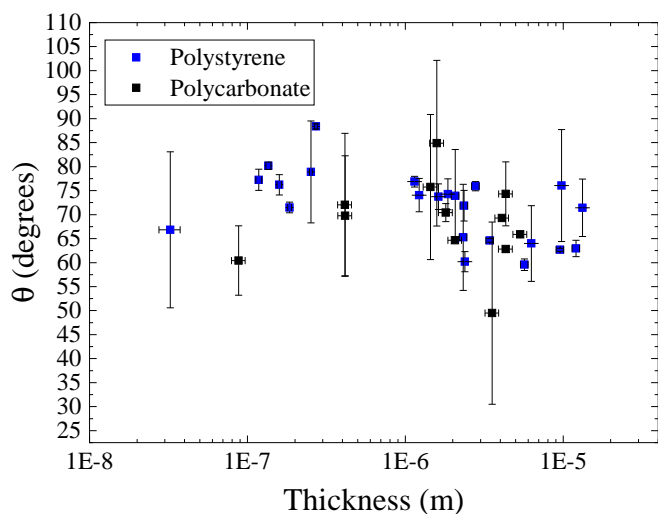

Fig. 3 θ as a function of film thickness. Both polystyrene and polycarbonate films show relatively constant behaviour. The average angles are 71$\pm$7 $^\circ$ and 69$\pm$9 $^\circ$ respectively.

flat and horizontal.

If the hypothesis that θ is always equal to θ_Y (or any constant) is correct, creating a force balance with observed angles and surface energies becomes problematic. Consider the result of a horizontal force balance, $\gamma \cos(\theta_Y) + (T + \gamma_{sl} + \gamma_{so}) \cos(\phi_1) = (T + \gamma_{sv} + \gamma_{so}) \cos(\phi_2)$, where γ_{so} refers to the surface tension of an oil/film interface, T to the tension acting on the ends of the plate, and the other variables remain as defined above. The relationship between the two angles ϕ_1 and ϕ_2 is further constrained by the vertical force balance, $\gamma \sin(\theta_Y) = (T + \gamma_{sl} + \gamma_{so}) \sin(\phi_1) + (T + \gamma_{sv} + \gamma_{so}) \sin(\phi_2)$, ultimately permitting a single solution (the Neumann solution). How then can the measured angles ϕ_1 and ϕ_2, which clearly vary with film thickness (see fig 2) be explained? Either we do not observe the true angles (ϕ_1 and ϕ_2), the measured constant value of θ is somehow incorrect (and θ is not θ_Y), or there are more than just surface forces acting at the triple point.

To proceed, we focus on the directly measured angle β, which is plotted as a function of film thickness in Fig. 4. The data shows a smooth monotonic increase in β as films thickness decreases for both PS and PC films. The good overlap of both materials is consistent with their similar surface energies and material properties, and is also a sign that films are undamaged during processing and over the course of the experiment. There are two independent physical limits for β. First, β must approach $\bar{\theta}_Y = \pi - \theta_Y$ at large thicknesses where the film does not bend. Second, in the absence of bending energy and external tension acting on the free end of the film, the film will come into self contact and $\beta = \pi/2 + \bar{\theta}_Y$. Measurements seem to indicate that this second limit is never reached experimentally. As discussed above, a simple force balance is insufficient to describe how β relates to surface forces, bending, and applied tension because a force balance does not include a moment balance around the triple line. The failure of simple force arguments is clear in the experimental variation of β with film thickness; no external forces or surface energies are related to thickness changes - only the bending moment relates to thickness. A comprehensive approach which correctly accounts for bending moments, external tension and substrate density is required to correctly describe observed contact angles.

Assuming the horizontal force balance occurs to set the contact angle locally, we treat the glycerol surface as a vertical line force of magnitude $\gamma \sin \theta_Y$ and model the system as a Euler-Bernoulli beam on a Winkler foundation.[30] The foundation stiffness is determined by the density of the oil bath, ρ and an external tension is supplied to the plate by the surface tension of the oil, T, pulling on the free end of the film. The result is the fourth order differential equation:

$$EIh''''(x) = \gamma\delta(x) + Th''(x) - \rho g h(x), \qquad (1)$$

where $h(x)$ represents the position of the film, E is the Young's modulus of the plate, and $I = t^3/12(1 - \nu^2)$ is the second moment of inertia per unit width. Film thickness and Poisson's ratio are denoted by t and ν, respectively.
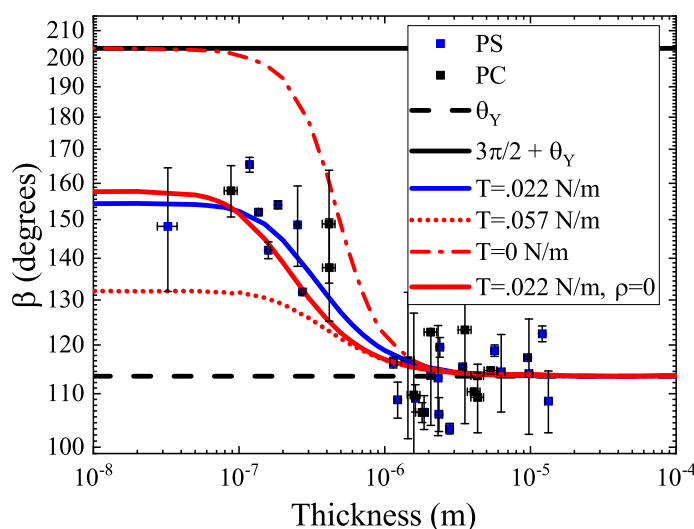
Fig. 4 The external angle β as a function of film thickness. Data for PS films (blue squares) and PC (black circles) are shown along with the output of the numerical model (red curves). The self-contact limit (solid black line) and the solid film (Young) limit (dashed black line) are also shown.

Fig. 5 Height as a function of position for ~ 100 nm (a,b) or ~ 1 μm (c,d) films. Figures a. and c. show a linear-log plot in which height has been normalized by its maximum value, in order for all curves to be visible. Figures b. and d. show the same data but with the height unnormalized and a log-log axis, again to facilitate viewing of all curves. a. and b. show data from a 200 nm PS film (black squares), and c. and d. show data from a 1.5 μm film (black squares again). Data shows good agreement even though none are 'fit' by the model.

Scaling analysis of Eqn. 1 reveals two important lengthscales. If the tension term is much larger than the gravitational term, we find the problem to be scaled by a length of $x_T \sim \sqrt{Et^3/T}$ (as has been pointed out for free-standing films).[25,29] In the opposite limit, we find a gravitational length of $x_G \sim (Et^3/\rho g)^{1/4}$ to dominate the problem.[31] Comparison of the two lengthscales defines a cross-over thickness, $t_c \sim (T^2/E\rho g)^{1/3}$, where the behaviour changes from gravity to tension dominated. Using the plane strain modulus of polystyrene $E = 3.9 \times 10^9$ Pa, the density and surface tension of the oil (1110 kg/m and 22 mN/m respectively) we predict a transition thickness of $t_c \sim 2.2\mu$m, which matches the thickness at which β deviates from the solid film limit observed experimentally.

If bending is ignored in Eqn. 1, a capillary length, $x_C \sim \sqrt{T/\rho g}$, emerges from a similar scaling analysis. Remarkably, the capillary length is equal to the gravitational and the tension lengths at t_c, highlighting the interdependence of externally applied tension, film bending, and gravity in the problem. Nevertheless, the contact angles are determined by the smallest observable lengthscale, which in this case is x_T when $t < t_c$. Bending cannot be ignored at experimentally relevant thicknesses (x_T is still greater than a micron for a 50 nm thick film). Even if the film were free of external tension, bending cannot be ignored because $x_C > x_G$ hence x_G is dominant at the contact line.

To gain further insight, we solve Eqn. 1 as a boundary value problem, and compare the numerical result with the experiment in several different ways. In Fig. 4 we overlay the previously discussed experimentally measured β values with the model predictions as a function of film thickness. Again, the angle was "measured" from numerically calculated shape profiles, which we show in figure 5. Here the model is compared to a typical thin and thick film (figure 5 a,b and c,d respectively). Finally, the last observable of note is the maximum height of the film which we show
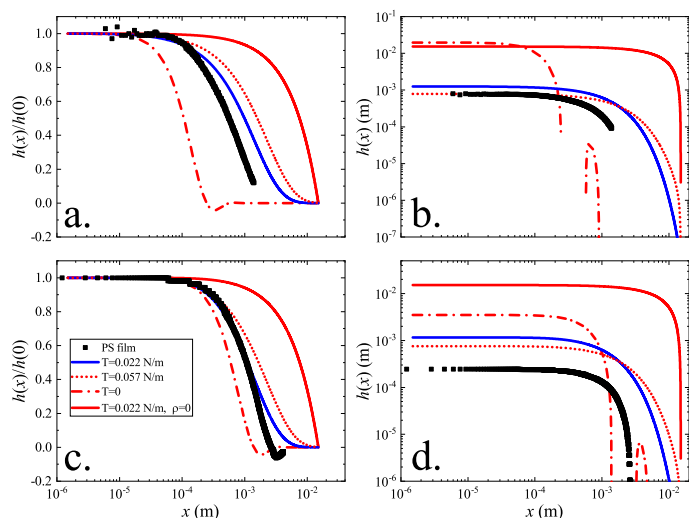
in figure 6 as a function of film thickness alongside experimental measurements. We numerically calculated four different curves, each motivated by different physical scenarios which we discuss in detail below. We note that the glycerol weight does shift the negative infinity plate boundary downwards, which can influence the apparent value of α, but has little baring on the overall peak height or the exterior angle β. Hence, we elect to use symmetric boundary conditions throughout (e.g.$h(\infty) = h(-\infty)$) in order to keep the analysis simple and focused on the contact point.

First, we calculate the zero gravity limit which eases comparison with existing free-standing film experiments ($\rho = 0$). The gravity free curve, assuming the external tension is still supplied by the oil phase surface tension, does fit the angular data. However, it is clearly not physically related to our experiment as can be seen in its profile (Fig. 5) or peak height (Fig. 6). The angular data smoothly changes from solid like (nearly constant) to a second limiting value as film thickness decreases. The transition at the lower thickness occurs because x_{obs} becomes greater than x_T, meaning the observation is not of high enough resolution to be influenced by x_T. It is now determined by a second lengthscale (in this case, the plate size L). The shape taken on by the film in the absence of a fluid substrate is nearly triangular; flat with an upward slope far from the contact line, curving only at a lengthscale comparable to x_T. The peak height is quite high (especially for thin films), and is strongly related to overall film length and the applied tension. The discrepancy between the measured and simulated peak heights is a clear sign that gravity plays a role in our experiment, whether films are thick or thin, and a zero gravity approximation is not applicable.

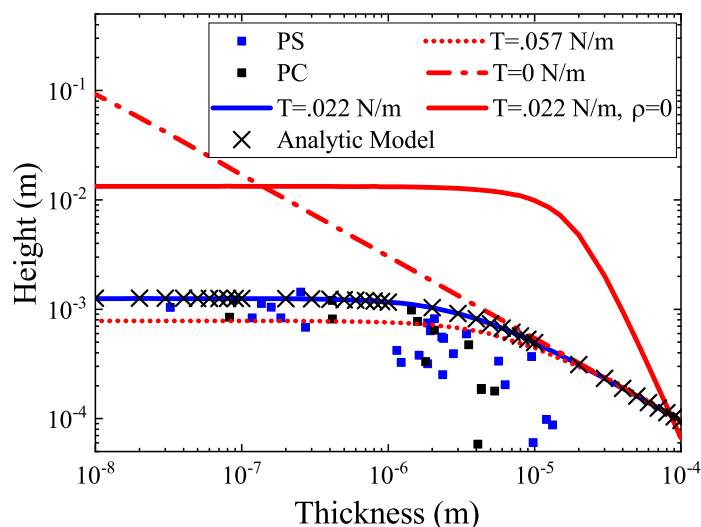Next we consider the contact line in the absence of an exter-

Fig. 6 Maximum height of the triple line as a function of film thickness for PS (blue squares) and PC (black circles) films. Numerical model results are shown for zero gravity, zero tension, and two other possible external tensions. Analytic model results are shown as X's.

nal tension (often the limit in which surface energies are measured [25,28,29]). Here we find β is considerably overestimated in comparison with the data, especially in the thin film limit where the film has come into self contact. In this case, as thickness decreases and x_{obs} falls below x_T, the film shape is governed by the gravitational lengthscale, x_G. The result is an increased drive to narrow the peak width. At larger thicknesses the angle approaches $\bar{\theta}_Y$ as is expected. The height of the lifted region of film (Fig. 6) follows a single power law, again deviating from the data considerably in the thin film limit. The power law can easily be explained by using the scaling length derived above, x_G, in combination with Eqn. 1 to derive a natural height $h_G \sim \gamma(\rho g)^{-3/4}(EI)^{-1/4}$. The agreement with the scaling clarifies how gravity plays a critical role over the entire range of film thicknesses in the zero tension limit.

Finally, in solid blue we show a curve generated using externally measured values for γ, T and ρ. This curve fits both the measured β (Fig. 4) and also fits the height data quite well (Fig. 6), with no additional free parameters. While not inconsistent with a low thickness β plateau, the data does not show a clear transition to 'thin'. This is likely due to the low brightness levels and tiny peak widths increasing error in our experiments coupled with the fragile nature of extremely thin films (fewer experiments survive processing). The height data is much more reliable in the thin film limit, but shows some deviation in the thick film limit (where β shows good agreement with the model). This is due to a combination of experimental effects, including plate lengths being comparable to the contact region width, and the weight of the fluid resting on the film altering the boundary conditions (we use symmetric hinge boundaries and large plates in the model). We additionally show model predictions for a film with a slightly larger tension to highlight the sensitivity of the experiment. In this case the low thickness β plateau occurs at a lower angle which is inconsistent with the data.

The beam model of Eqn. 1 can be supplemented by calculating similar height profiles from a free-energy based capillary model (see Appendix A). This method has the advantage of producing simple, analytic results for various measured properties and removes some of the complexity of a full continuum theory. For the sake of clarity, we only focus on the maximum height of the deformation and contact angle (β) in this work. Assuming a zero derivative boundary at the deformation peak (consistent with our interpretation of the true contact point), we find the peak height as a function of thickness to be:

$$h_0 = x_C \frac{\gamma}{2\gamma_S} \frac{1}{\sqrt{1+2(x_G^2/x_C^2)}}. \qquad (2)$$

where γ_s is the surface energy associated with moving the plate upwards and increasing the surface length. Because the plate's extension is tiny, we ignore any change in plate length and associate γ_s with T the surface tension of the oil bath. Eqn. 2 is plotted in Fig. 6 alongside earlier numerical results, and the agreement is near perfect. This shows that there is no difference between energy-based or force-based models, and again highlights the interdependence of gravity, tension, and bending in our experiment.

The contact angle in this model is simply θ_Y by construction (e.g. the zero derivative boundary condition at the deformation peak). However, as experimental angles are measured a distance away from the true contact line (x_{obs}), the true contact angle is is not observed directly. Again, as with the numerical model, we can derive an apparent angle from the predicted curve shape. In this case, we can proceed analytically by using the derivative of the film shape (shown in the appendix) calculated at x_{obs}. Fig. 7 shows the resulting β plotted alongside the PC and PS data with the numerical 'fit' to ease comparison. The analytic result is in good agreement with the numerical model and what is observed in the experiment. The two results do not prove that the true contact angle is always θ_Y, but do show that the experiments are at least consistent with this hypothesis.

4 Conclusions

We have examined the microscopic details of a fluid/thin-film contact line using confocal microscopy. We find that gravity, external tension, and bending are all important in the region of film thicknesses examined ($\sim 1 \times 10^{-8}$ to $\sim 1 \times 10^{-5}$ m). The experimentally measured angles, film shapes and peak heights show good agreement with with a Euler-Bernoulli beam or an equivalent, analytic, capillary model. Our results show that a tension only force balance, as in the Neumann construction, is not possible over most of the range of our experiments. Films with thicknesses above 100 nm have too much bending to consistently satisfy such a model, largely because the concept of a contact angle is ill defined. We suggest that, a Young-Dupré force balance always takes place on an extremely local scale (though a scale larger than molecular sizes). The contact may not be observable if the radius of curvature of the film falls below optically observable lengthscales. As film thicknesses increase, so does the radius of curvature, which leads to imprecise contact angles which are not useful in determining a force balance. Eventually, bend-
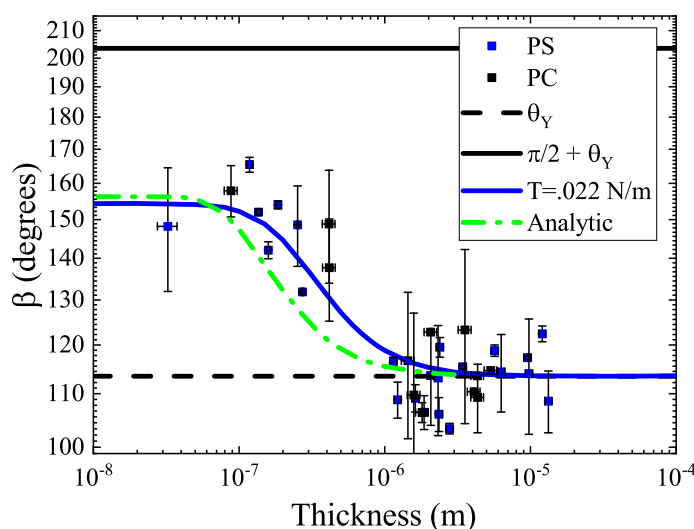
Fig. 7 The external angle β as a function of film thickness reproduced to clarify demonstration of the analytic theory discussed in the text. Data for PS films (blue squares) and PC (black circles) are shown along with the output of the optimal numerical model (blue curve). Analytic theory calculated with a $5\mu m$ observation length is shown by the dash-dotted green curve.

ing completely dominates, the film remains globally flat, and a Young-Dupré horizontal force balance is macroscopically observable.

5 Acknowledgements

A The Capillary Model

A capillary model can be constructed to describe the free energy of a fluid resting on a thin film in one dimension. Minimizing the difference in free-energy per unit width before and after the film is deformed allows analytic solutions to be developed in several useful situations. From this point of view, each surface contributes a term to the free energy which is proportional to its surface energy, and its surface area, A. For example, the fluid resting on top of the film has a free energy, $\int \gamma dA$ which can be reduced if the film is lifted and decreases the fluid/air interfacial area. The fluid bath beneath the film is lifted if the film is deformed above the horizontal plane and thus contributes a term proportional to the height of the deformation and the density, ρ, of the fluid bath ($\rho g \int dx \int h(x)dh$). The bending of the film as it is lifted also adds energy per unit width of film, $U_B = B/2 \int \kappa^2 dx$ where κ is the film's curvature, $B = EI = Et^3/12(1-\nu^2)$ is the bending modulus with film thickness t and Poisson ratio ν. Assuming, for simplicity, the problem is symmetric about the origin $x = 0$ and all deformations are small, the total change in free energy per unit width can be written:

$$\Delta F = -\gamma h_0 + \frac{\gamma_S}{2} \int_{-\infty}^{\infty} h'^2 dx + \frac{\rho g}{2} \int_{-\infty}^{\infty} h^2 dx + \frac{B}{2} \int_{-\infty}^{\infty} h''^2 dx, \quad (3)$$

where h_0 is the film height at the origin (we assume a purely vertical fluid surface lifting the film), γ is the surface tension of the top fluid, and γ_S is the net surface energy change of the film and oil interface. Using the capillary length, $x_C = \sqrt{\gamma_S/\rho g}$ and the gravitational length $x_G = (EI/\rho g)^{1/4}$, Eqn. 3 can be simplified to:

$$\Delta F = -\gamma h_0 + \frac{\rho g}{2} \int_{-\infty}^{\infty} \left[x_C^2 h'^2 + h^2 + x_G^4 h''^2 \right] dx. \quad (4)$$

Eqn. 4 is minimized when the differential equation,

$$h - x_C^2 h'' + x_G^4 h'''' = 0, \quad (5)$$

is satisfied. Subject to the symmetry requirement $h(x) = h(-x)$ and the boundary conditions $h(0) = h_0$, $h'(0) = 0$, $h(x \to \infty) = h'(x \to \infty) = 0$ the solution for $x \geq 0$ is given by

$$h(x) = \frac{h_0}{w_1 - w_2} \left(w_1 e^{-w_2 x} - w_2 e^{-w_1 x} \right), \quad (6)$$

where the inverse lengths w_1 and w_2 are related to the two rival lengthscales x_C anbd x_G through $w_1^2 w_2^2 = 1/x_G^4$ and $1/w_1^2 + 1/w_2^2 = x_C^2$. Inserting the solution back into ΔF and minimizing with respect to h_0 yields for the optimal height at the origin

$$h_0 = x_C \frac{\gamma}{2\gamma_S} \frac{1}{\sqrt{1 + 2(x_G^2/x_C^2)}}. \quad (7)$$

A second useful expression, the slope of the curve, allows a determination of any apparent contact angle of interest. The slope of Eqn. 6 is simply its derivative, given by

$$h'(x) = \frac{h_0}{w_1 - w_2} w_1 w_2 \left(-e^{-w_2 x} + e^{-w_1 x} \right). \quad (8)$$

For example, we use Eqn. 8 to calculate a contact angle for films of thickness ranging from 3 μm to 10 nm at a point $x = 5$ μm, which is shown in figure 7.

References

1 A. Terfort, N. Bowden and G. Whitesides, *Nature*, 1997, **386**, 162–164.

2 C. Py, P. Reverdy, L. Doppler, J. Bico, B. Roman and C. N. Baroud, *Phys. Rev. Lett.*, 2007, **98**, 156103.

3 C. Py, P. Reverdy, L. Doppler, J. Bico, B. Roman and C. Baroud, *Euro. Phys. J. Spec. Top.*, 2009, **166**, 67–71.

4 R. Pericet-Cámara, A. Best, H.-J. Butt and E. Bonaccurso, *Langmuir*, 2008, **24**, 10565–10568.

5 M. Shanahan and A. Carre, *Langmuir*, 1995, **11**, 1396–1402.

6 C. Extrand and Y. Kumagai, *Journal of colloid and interface science*, 1996, **184**, 191–200.

7 E. R. Jerison, Y. Xu, L. A. Wilen and E. R. Dufresne, *Phys. Rev. Lett.*, 2011, **106**, 186103.

8 R. W. Style and E. R. Dufresne, *Soft Matter*, 2012, **8**, 7177–7184.

9 R. W. Style, R. Boltyanskiy, Y. Che, J. Wettlaufer, L. A. Wilen and E. R. Dufresne, *Phys. Rev. Lett.*, 2013, **110**, 066103.

10 Q. Xu, R. W. Style and E. R. Dufresne, *Soft Matter*, 2018, **14**, 916–920.

11 J. T. Pham, F. Schellenberger, M. Kappl and H.-J. Butt, *Phys. Rev. Mat.*, 2017, **1**, 015602.

12 R. W. Style, C. Hyland, R. Boltyanskiy, J. S. Wettlaufer and E. R. Dufresne, *Nat. Comm.*, 2013, **4**, 2728.

13 C. Y. Hui, A. Jagota, Y. Y. Lin and E. J. Kramer, *Langmuir*, 2002, **18**, 1394–1407.

14 S. Mora, T. Phou, J.-M. Fromental, L. M. Pismen and Y. Pomeau, *Phys. Rev. Lett.*, 2010, **105**, 214301.

15 B. Andreotti, O. Bäumchen, F. Boulogne, K. E. Daniels, E. R. Dufresne, H. Perrin, T. Salez, J. H. Snoeijer and R. W. Style, *Soft Matter*, 2016, **12**, 2993–2996.

16 R. W. Style, A. Jagota, C.-Y. Hui and E. R. Dufresne, *Annu. Rev. of Cond. Matt. Phys.*, 2017, **8**, 99–118.

17 J. Bae, T. Ouchi and R. C. Hayward, *ACS Appl. Mat. Int.*, 2015, **7**, 14734–14742.

18 J. Huang, M. Juszkiewicz, W. H. De Jeu, E. Cerda, T. Emrick, N. Menon and T. P. Russell, *Science*, 2007, **317**, 650–653.

19 R. Schroll, M. Adda-Bedia, E. Cerda, J. Huang, N. Menon, T. Russell, K. Toga, D. Vella and B. Davidovitch, *Phys. Rev. Lett.*, 2013, **111**, 014301.

20 J. D. Paulsen, E. Hohlfeld, H. King, J. Huang, Z. Qiu, T. P. Russell, N. Menon, D. Vella and B. Davidovitch, *Proc. Nat. Acad. Sci.*, 2016, **113**, 1144–1149.

21 J. D. Paulsen, V. Démery, K. B. Toga, Z. Qiu, T. P. Russell, B. Davidovitch and N. Menon, *Phys. Rev. Lett.*, 2017, **118**, 048004.

22 J. D. Paulsen, V. Démery, C. Santangelo, R. T.P., B. Davidovitch and N. Mennon, *Nat. Mat.*, 2015, **14**, 1206–1209.

23 D. Kumar, J. D. Paulsen, R. T.P. and N. Mennon, *Science*, 2018, **359**, 775–778.

24 B. Davidovitch and D. Vella, *Soft Matter*, 2018, **14**, 4913–4934.

25 R. D. Schulman and K. Dalnoki-Veress, *Phys. Rev. Lett.*, 2015, **115**, 206101.

26 R. D. Schulman, R. Ledesma-Alonso, T. Salez, Raphaël and K. Dalnoki-Veress, *Phys. Rev. Lett.*, 2015, **118**, 198002.

27 R. D. Schulman, M. Trejo, T. Salez, Raphaël and K. Dalnoki-Veress, *Nat. Comm.*, 2018, **9**, 982.

28 N. Nadermann, C.-Y. Hui and A. Jagota, *Proc. Nat. Acad. Sci.*, 2013, **110**, 10541–10545.

29 C.-Y. Hui and A. Jagota, *Proc. R. Soc. A*, 2014, **470**, 20140085.

30 D. A. Dillard, B. Mukherjee, P. Karnal, R. C. Batra and J. Frechette, *Soft Matter*, 2018, **14**, 3669–3683.

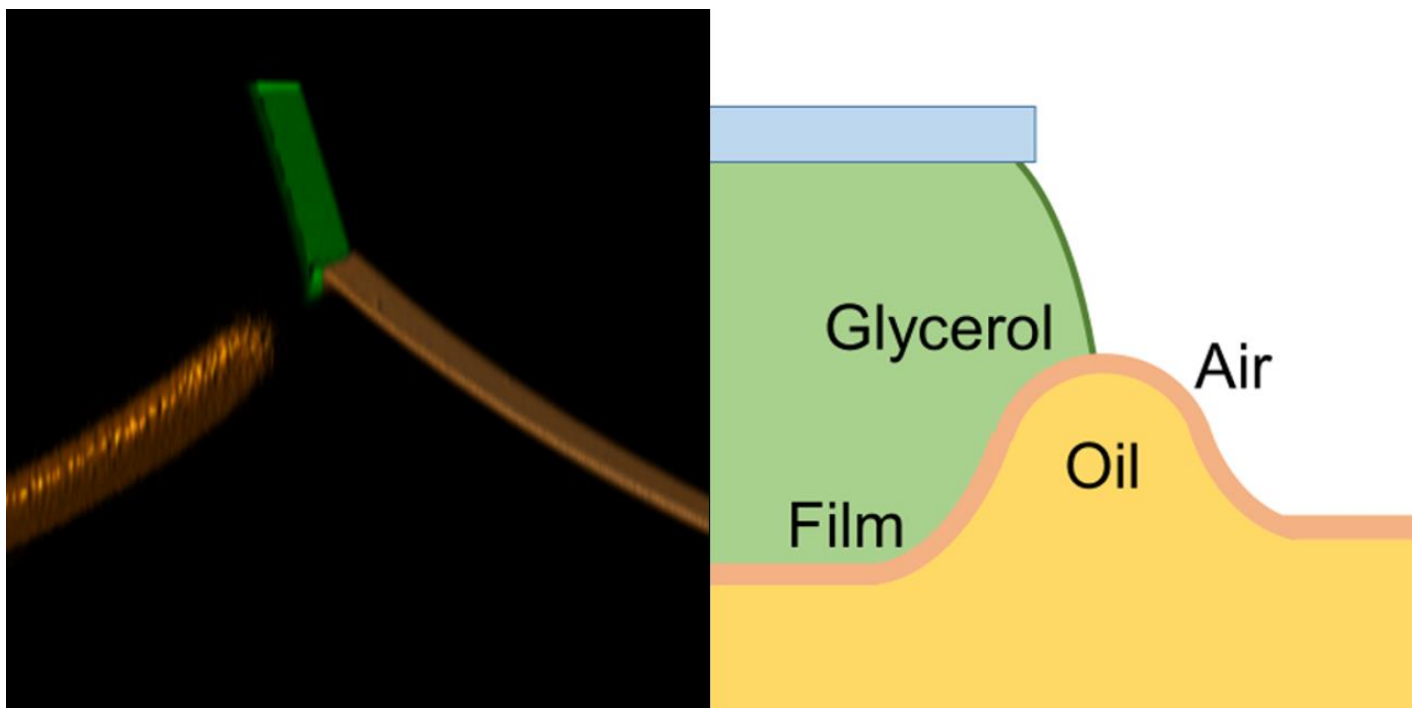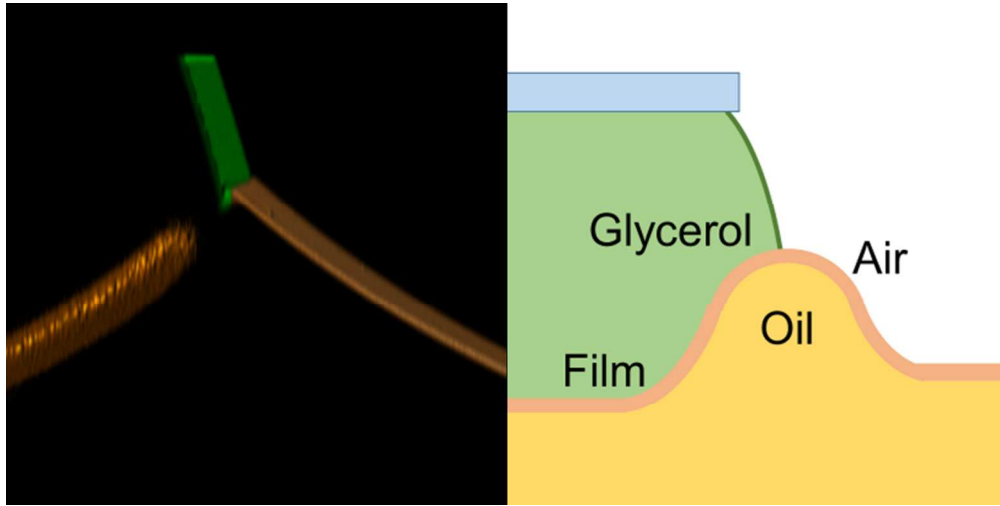31 E. Cerda and L. Mahadevan, *Phys. Rev. Lett.*, 2003, **90**, 074302.

Fig. 8 A microscopic study of slender but rigid polymer film deformed by a liquid droplet contact line

451x225mm (72 x 72 DPI)